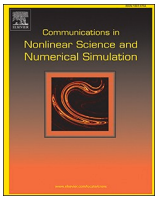
Commun Nonlinear Sci Numer Simulat 161 (2026) 110171



Contents lists available at ScienceDirect

Communications in Nonlinear Science and Numerical Simulation

journal homepage: www.elsevier.com/locate/cnsns



Research paper

Chaos emergence in structures with seismic isolation bearings



Vladimir Bratov [a,*], Ashraf M. Iqbal [b], Sergey V. Kuznetsov [c]

[a] Edinburgh Napier University, Edinburgh, UK
[b] Indian Institute of Technology Roorkee, Roorkee, India
[c] Moscow State University of Civil Engineering, Moscow, Russia

ARTICLE INFO

Keywords:
Hyperelastic material
Vibration
Chaos
Quasi-periodic motion
Subharmonic oscillations
Amplitude spectrum

ABSTRACT

This study demonstrates that a modified Kelvin–Voigt oscillator incorporating a nonlinear spring element governed by the Ogden hyperelastic potential—representative of elastomeric seismic bearings composed of hard rubber—can exhibit chaotic vibration behavior under certain excitation conditions. The results reveal that these chaotic responses contain pronounced subharmonic and broadband continuous spectral components, which may amplify structural motion and compromise the protective effectiveness of seismic isolation systems. To investigate this phenomenon, the system dynamics are formulated as an autonomous set of three coupled first-order differential equations and solved numerically using the Adams–Bashforth–Moulton (ABM) predictor–corrector scheme, well-suited for stiff nonlinear systems. The analysis provides new insight into the complex vibrational behavior of rubber-based seismic and vibration isolation devices modeled by Ogden-type hyperelastic potentials, highlighting the importance of nonlinear material effects in the dynamic stability of protected structures.

1. Introduction

1.1. Problem statement

Herein, following [1–7], a modified Kelvin – Voigt model with a nonlinear spring element is considered; see Fig. 1.
The equation of motion for the considered model can be written in the form [8]

$$m\ddot{x} = -\eta\dot{x} - k(x) + f\cos(\omega t) \tag{1.1}$$

where m is the mass; η is the linear viscous coefficient; $k(x)$ is the nonlinear stiffness; f is the amplitude of the driving force; ω is the angular frequency; and t is the time.

The current study relies on the Ogden hyperelastic potential to model the nonlinear behavior of seismic bearings under large excitations resembling high-intensity seismic waves. Note that the Ogden potential is widely used to model various cross-linked polymers, including the hard rubber employed in seismic protection devices [9–13]. The principal outcome of this research is the observation of chaotic oscillations occurring under variations of physical parameters. As shown, these excitations lead to the emergence of subharmonic and superharmonic continuous spectral components, which can dramatically alter the response of the protected structure. By integrating the Ogden hyperelastic potential into a modified Kelvin–Voigt oscillator, the work captures essential material

* Corresponding author.
E-mail addresses: v.bratov@napier.ac.uk (V. Bratov), ashraf.iqbal@ce.iitr.ac.in (A.M. Iqbal), kuzn-sergey@yandex.ru (S.V. Kuznetsov).

https://doi.org/10.1016/j.cnsns.2026.110171
Received 11 December 2025; Received in revised form 2 March 2026; Accepted 21 May 2026
Available online 22 May 2026
1007-5704/© 2026 The Author(s). Published by Elsevier B.V. This is an open access article under the CC BY license (http://creativecommons.org/licenses/by/4.0/).

nonlinearities characteristic of hard-rubber seismic bearings—features that are typically oversimplified or omitted in conventional models. The analysis demonstrates, for the first time, that such systems can exhibit strongly chaotic responses with rich subharmonic and broadband spectral content, revealing dynamic behaviors that may critically influence the performance and reliability of seismic isolation devices.

1.2. Overview

1.2.1. Ogden hyperelastic potential

The Ogden hyperelastic potential [14,15] for an incompressible medium, modeling rubber, can be written in the form

$$W(\lambda_1,\lambda_2,\lambda_3)=\sum_{n=1}^{N}\frac{\mu_n}{\alpha_n}\left(\sum_{k=1}^{3}\lambda_k^{\alpha_n}-3\right) \tag{1.2}$$

where μ_n are the hyperelastic moduli; α_n are not necessarily integer exponents; and $\lambda_k,\quad k=1,2,3$ are the principal stretches, satisfying the incompressibility condition [14]

$$\left(\prod_{k=1}^{3}\lambda_k\right)=1 \tag{1.3}$$

More general forms of the Ogden potential (1.2) are also known – for example, the Valanis – Landel models [16], to which the Ogden potential (1.2) belongs as a special case; see also more recent works [17–19]

Potential (1.2) yields the following principal stresses [20]

$$\sigma_k\equiv -p+\lambda_k\frac{\partial W}{\partial\lambda_k}=-p+\sum_{n=1}^{N}\mu_n\lambda_k^{\alpha_n} \tag{1.4}$$

no summation over repeated index k is assumed in this equation.

Based on fitting material constants in (1.2) to experimental data, it was proposed [21,22] a simpler form of the Ogden potential containing only one term

$$\mu_1=\mu;\alpha_1=\alpha \tag{1.5}$$

The hyperelastic potential (1.2), along with its special case (1.5), is widely used to model the nonlinear elastic behavior of various cross-linked polymers, including natural rubber, due to its (i) ability to accurately capture stress–strain relationships under both

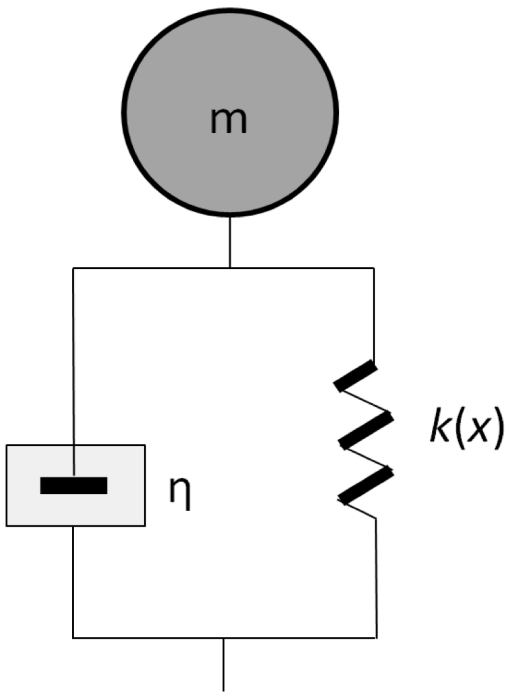


Fig. 1. Modified Kelvin – Voigt model with nonlinear spring element: m is the mass; η is the linear viscos damping coefficient; $k(x)$ is the nonlinear stiffness.

compressive and tensile loading conditions; and (ii) suitability for modeling nearly incompressible media, to which cross-linked polymers in the glassy state primarily belong; see [23–30,21,31–33].

1.2.2. Pure shear

A typical elastomeric seismic bearing undergoes pure shear strain during a seismic event [34]. Adopting a modified Kelvin – Voigt model with a nonlinear spring element governed by the Ogden hyperelastic potential (1.2) subject to constraint (1.3), and assuming pure shear strain, yields [20]:

$$\lambda_1 = (1+e); \lambda_2 = (1-e); \lambda_3 = \left(1-e^2\right)^{-1} \tag{1.6}$$

where e is the nominal strain [20], $e > 1$. In view of Eq. (1.4) this gives:

$$\sigma_1 \equiv -p + \sum_{n=1}^{N} \mu_n (1+e)^{\alpha_n}; \sigma_2 \equiv -p + \sum_{n=1}^{N} \mu_n (1-e)^{\alpha_n}; \sigma_3 \equiv -p + \sum_{n=1}^{N} \mu_n \left(1-e^2\right)^{-\alpha_n} \tag{1.7}$$

In the considered case, the boundary conditions can be written as [34]:

$$\sigma_3 = 0 \tag{1.8}$$

from where [35]

$$\sigma_1 \equiv \sum_{n=1}^{N} \mu_n \left((1+e)^{\alpha_n} - \left(1-e^2\right)^{-\alpha_n}\right); \sigma_2 \equiv \sum_{n=1}^{N} \mu_n \left((1-e)^{\alpha_n} - \left(1-e^2\right)^{-\alpha_n}\right) \tag{1.9}$$

The latter expression, together with the one-term potential (1.5), will be used in the subsequent analysis.

1.2.3. Ogden oscillator

To construct the Ogden oscillator, denote the nominal strain $e = x$

$$\lambda_{1,2} = 1 \pm x \tag{1.10}$$

where x demotes the corresponding strain. Now, following [1,2] and taking into account Eq. (1.9) and Eq. (1.10), the nonlinear force in Eq. (1.1) becomes

$$k(x) \equiv \sum_{n=1}^{N} \mu_n \left((1 \pm (x-u))^{\alpha_n} - \left(1-(x-u)^2\right)^{-\alpha_n}\right) \tag{1.11}$$

where $u$corresponds to the displacement of the foundation [1]:

$$u(t) = u_0 \cos(\omega t) \tag{1.12}$$

and u_0 is the corresponding amplitude. Not that the signs $\pm$ in Eq. (1.11) are irrelevant for the further analysis. Bearing in mind Eq. (1.11) and the viscous damping force $\eta(\dot{x} - \dot{u})$, the equation of motion becomes

$$m\ddot{x} = -\eta(\dot{x} - \dot{u}) - k(x-u) \tag{1.13}$$

where the external loading is replaced by the displacement of a foundation.

Following Ueda [36–39], introduce a dimensionless time variable

$$\tau = \omega t \tag{1.14}$$

which allows us to rewrite Eq. (1.13):

$$\ddot{x}_{\tau\tau} = -\eta'(\dot{x}_\tau - \dot{u}_\tau) - k'(x-u) \tag{1.15}$$

where the subscript τ-indices, denotes differentiation with respect to τ, and

$$\eta' = \frac{\eta}{m\omega}; k' = \frac{k}{m\omega^2} \tag{1.16}$$

Here after, the prime notation and subscript τ will be omitted for clarity.

The equations, similar to (1.15), appear in various studies related to the analysis of oscillations in nonlinear dynamical systems [40–43]. It should also be noted that along with single-degree-of-freedom models, a number of works investigate forced vibrations of nonlinear beams [44], plates [45], and shells [46], where chaotic behavior is also observed. Another remark concerns the nonlinearities incorporated in various Kelvin – Voigt models. To the best of authors' knowledge, none of the existing studies on nonlinear oscillators has employed Ogden-type hyperelastic potentials to represent the spring nonlinearity.

2. Governing equations

2.1. Equations of state

Here after, following [21,22], the elastic force will be adopted in the one-modulus form (1.5):

$$k(x) \equiv \mu\left((1+x-u)^{\alpha} - \left(1-(x-u)^2\right)^{-\alpha}\right) \tag{2.1}$$

The tangent modulus, defined by differentiating Eq. (2.1), becomes

$$E(x) \equiv \partial_x k(x) = \alpha\mu\left((1+(x-u))^{\alpha-1} + \left(1-(x-u)^2\right)^{-\alpha-1}\right) \tag{2.2}$$

The last expression shows that $E(x) > 0$ for any x, ensuring that the material remains mechanically stable throughout the domain

$$-1 < x - u < 1 \tag{2.3}$$

of admissible values of x [20] and that the hyperbolicity of equation of motion (1.15) remains at any x within the range (2.3).

2.2. Equations of motion

2.2.1. Non-autonomous dynamical system

Eq. (1.13) can be expressed in the form of a first-order non-autonomous dynamical system:

$$\dot{X} = G(X,\tau) \tag{2.4}$$

where

$$X = \begin{pmatrix} x \\ v \end{pmatrix}; G(X) = \begin{pmatrix} v \\ -k(x-u) - \eta(v-\dot{u}) \end{pmatrix} \tag{2.5}$$

and $v = \dot{x}$.

Taking the gradient of matrix G with respect to the variable X, yields the Jacobian matrix [47]:

$$J(X) \equiv \nabla_X G(X) = \begin{pmatrix} 0 & 1 \\ -E(x-u) & -\eta \end{pmatrix} \tag{2.6}$$

from where the eigenvalues can be derived

$$e_{1,2}(x) = \frac{-\eta \pm \sqrt{\eta^2 - 4E(x)}}{2} \tag{2.7}$$

Assuming $4E(x) > \eta^2$, which is natural for rubber-like materials used in seismic isolators, the stiffness indicator s of the considered dynamical system becomes [48,49]:

$$s \equiv \frac{\max|\mathrm{Re}(e_i)|}{\min|\mathrm{Re}(e_j)|} = 1 \tag{2.8}$$

According to [48], the latter means that the dynamical system (2.4) is non-stiff. However, to get a more reliable estimate, transition to the autonomous system is needed [48–50].

2.2.2. Autonomous dynamical system

Following [47], introduce a new scalar variable

$$w = \cos(\tau) \tag{2.9}$$

and two 3-vectors

$$X = \begin{pmatrix} x \\ v \\ w \end{pmatrix}; G(X) = \begin{pmatrix} v \\ -k(x-u_0 w) - \eta\left(v \mp u_0\sqrt{1-w^2}\right) \\ \pm\sqrt{1-w^2} \end{pmatrix} \tag{2.10}$$

With these vectors, the autonomous dynamical system takes the form

$$\dot{X} = G(X) \tag{2.11}$$

Now the time variable does not explicitly enter Eq. (2.11).

Taking the gradient of G with respect to X, gives the Jacobian matrix

$$J(X) \equiv \nabla_X G(X) = \begin{pmatrix} 0 & 1 & 0 \\ -E(x-u_0 w) & -\eta & \mp u_0 \eta \left(1-w^2\right)^{-1/2} \\ 0 & 0 & \pm w\left(1-w^2\right)^{-1/2} \end{pmatrix} \tag{2.12}$$

The eigenvalues of matrix J are as follows

$$e_{1,2}(x) = \frac{-\eta \pm \sqrt{\eta^2 - 4E(x)}}{2}; e_3 = \pm \frac{w}{\sqrt{1-w^2}} \tag{2.13}$$

The last expression reveals that $|e_3| \to \infty$ at $w \to \pm 1$, meaning the stiffness ratio becomes infinite, and, hence, the system should be considered as stiff, making the use of explicit solvers inapplicable.

2.3. Adams–bashforth–moulton (ABM) method

To integrate autonomous dynamical system (2.10), the explicit–implicit Adams–Bashforth–Moulton (ABM) variable step-size method is employed [48,51–53]. In this work, a fourth-order ABM predictor–corrector scheme is employed. This formulation consists of a three-step Adams–Bashforth predictor followed by a four-step Adams–Moulton corrector, which together yield an overall fourth-order accurate integration method. Although the considered ABM scheme is not fully A-stable, the presence of the implicit Moulton corrector gives it a significantly larger stability region than explicit Runge–Kutta methods of comparable order. This expanded stability domain makes ABM more resilient to step-size-induced instabilities and better suited for long-time integrations of moderately stiff systems; see [48,53].

2.3.1. Predictor (adams-bashforth explicit step)

The explicit step of the considered method relies on N previous steps:

$$Y_{n+1} = Y_n + h\left(\sum_{k=1}^{N} a_k (K(Y_{n+1-k}))\right) \tag{2.14}$$

where

$$Y_k = Y(t_k); h = t_{k+1} - t_k \tag{2.15}$$

and intergrating coefficients a_k depend on the number of steps N in the integrating scheme. The coefficients a_k depend on the order of the Lagrange interpolation polynomial [48,54]:

$$\begin{aligned} &N=1: \quad a_1 = 1 \\ &N=2: \quad a_1 = \frac{3}{2}; \quad a_2 = -\frac{1}{2} \\ &N=3: \quad a_1 = \frac{23}{12}; \quad a_2 = -\frac{16}{12}; \quad a_3 = \frac{5}{12} \end{aligned} \tag{2.16}$$

2.3.2. Corrector (adams-moulton implicit step)

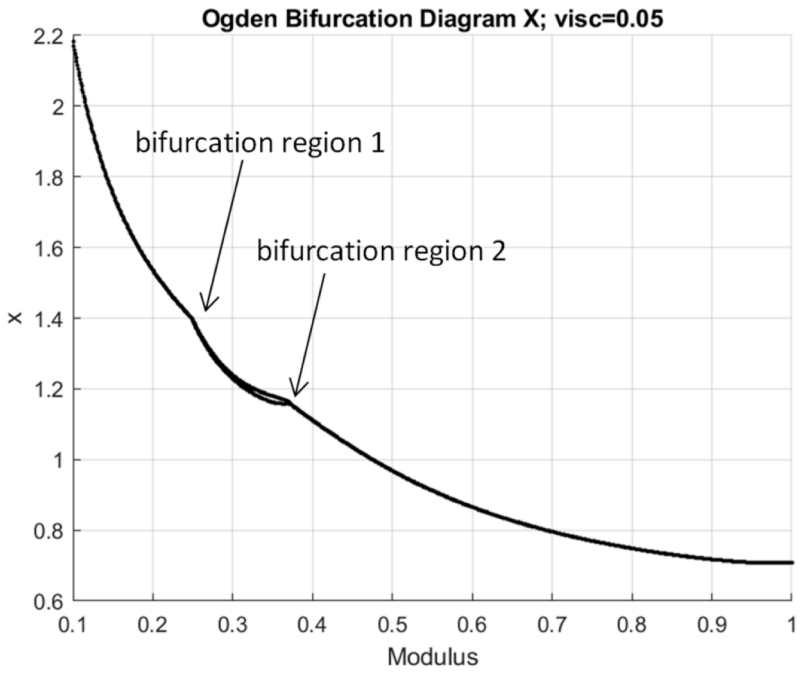
The imlicit step relies on the following equation [48,55,54]

$$Y_{n+1} = Y_n + h\left(\sum_{k=0}^{N} b_k (K(Y_{n+1-k}))\right) \tag{2.17}$$

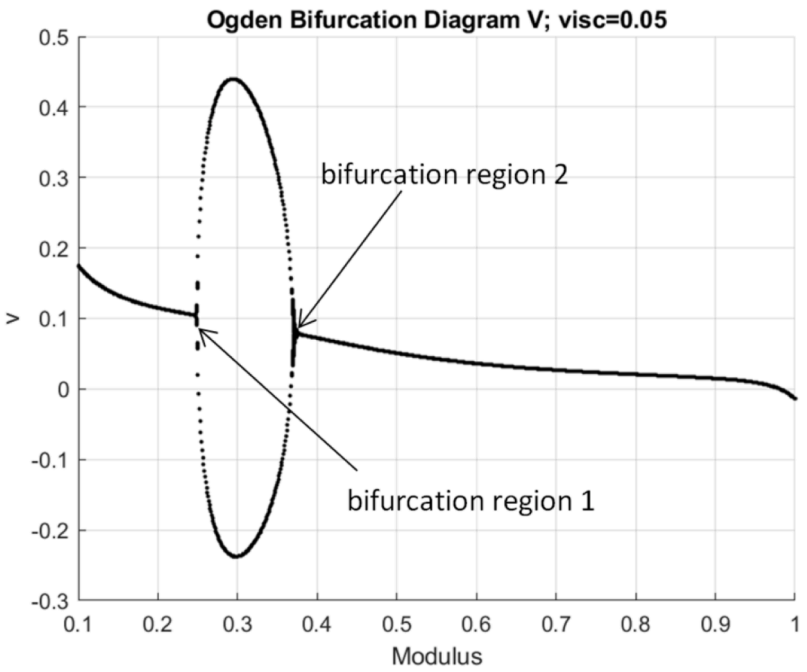
Now, the integrating coefficients become [48]

$$\begin{aligned} &N=1: \quad b_0 = \frac{1}{2}; \quad b_1 = \frac{1}{2} \\ &N=2: \quad b_0 = \frac{5}{12}; \quad b_1 = \frac{8}{2}; \quad b_2 = -\frac{1}{12} \\ &N=3: \quad b_0 = \frac{9}{24}; \quad b_1 = \frac{19}{24}; \quad b_2 = -\frac{5}{24}; \quad b_3 = \frac{1}{24} \\ &N=4: \quad b_0 = \frac{251}{720}; \quad b_1 = \frac{646}{720}; \quad b_2 = -\frac{264}{720}; \quad b_3 = \frac{106}{720}; \quad b_4 = -\frac{19}{720} \end{aligned} \tag{2.18}$$

These coefficients, as in the previous case, depend upon the order of the Lagrange interpolation polynomial.

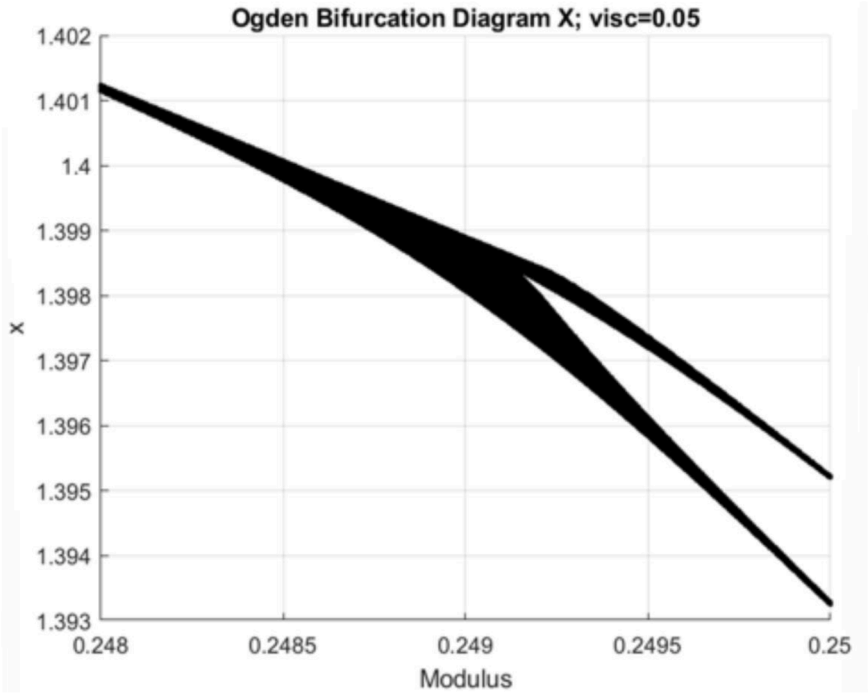


a)

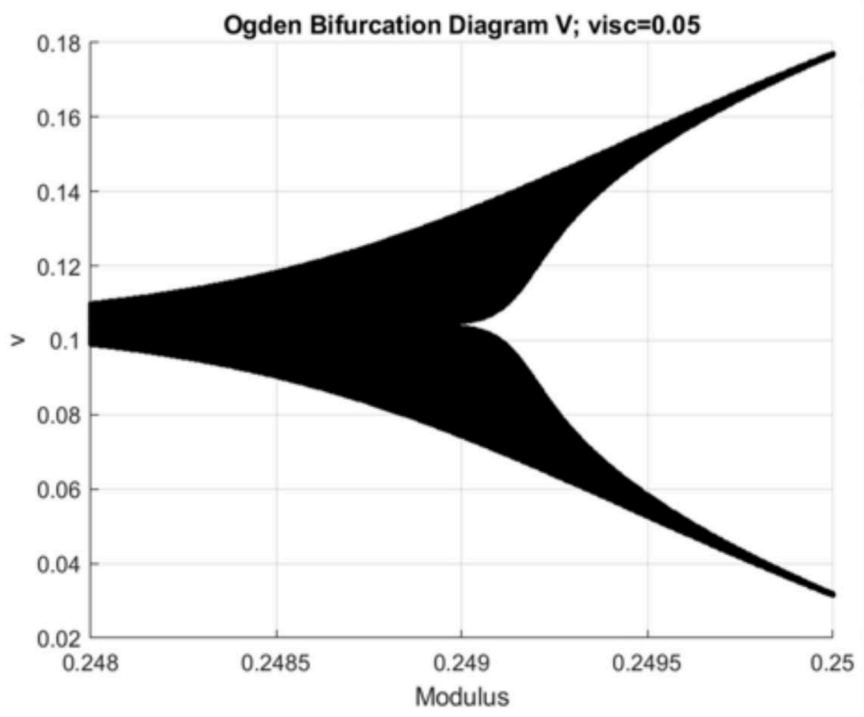


b)

Fig. 2. Bifurcation diagrams over modulus μ variation: a) x-diagram; b) v-diagram.

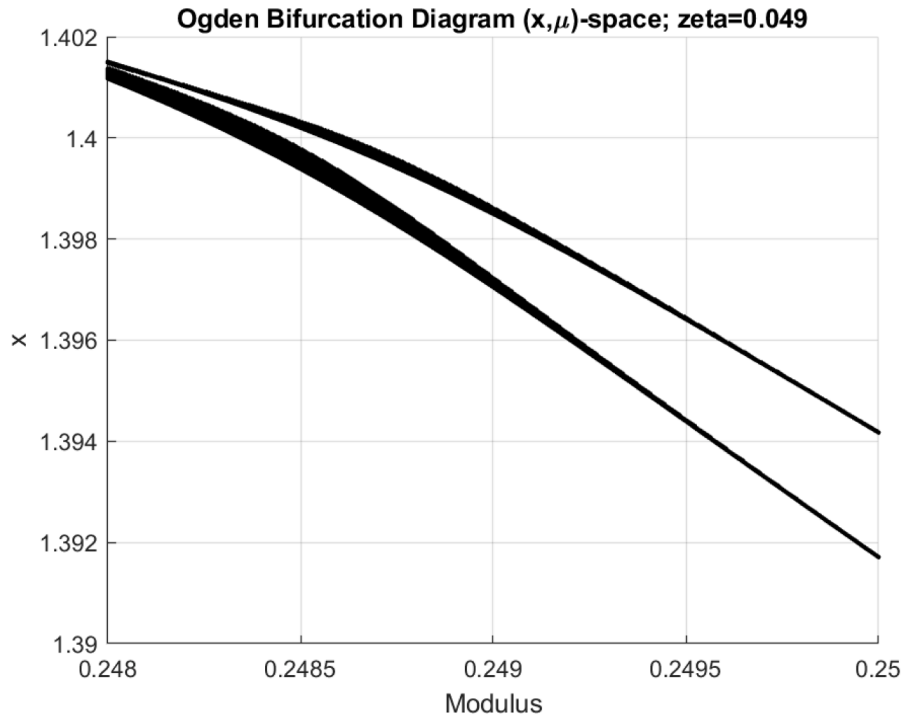


a)

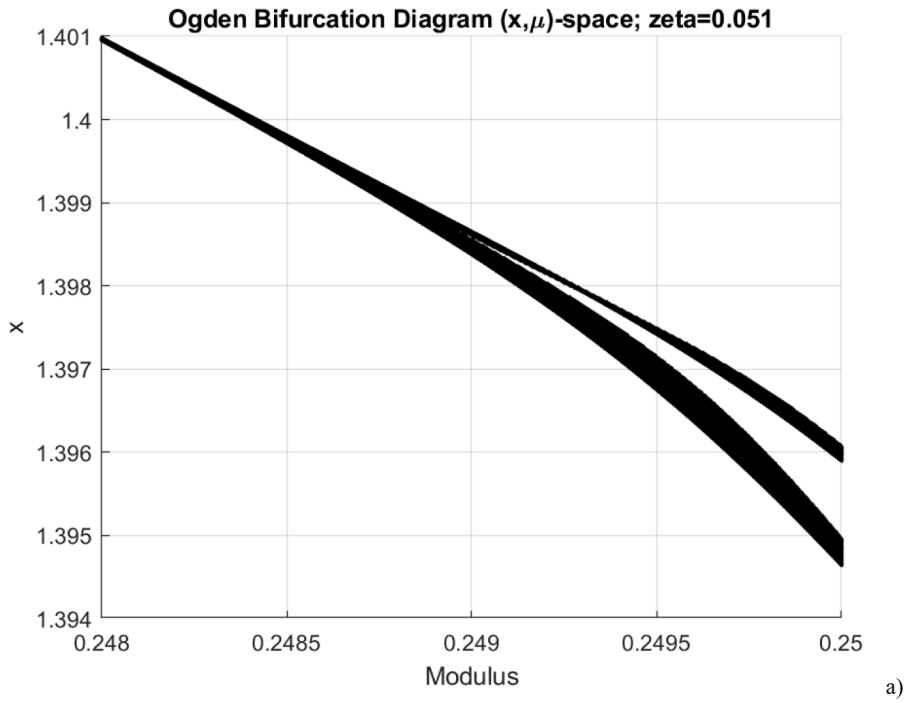


b)

Fig. 3. Bifurcation diagrams in the vicinity of the first bifurcation region: a) x-diagram; b) v-diagram.

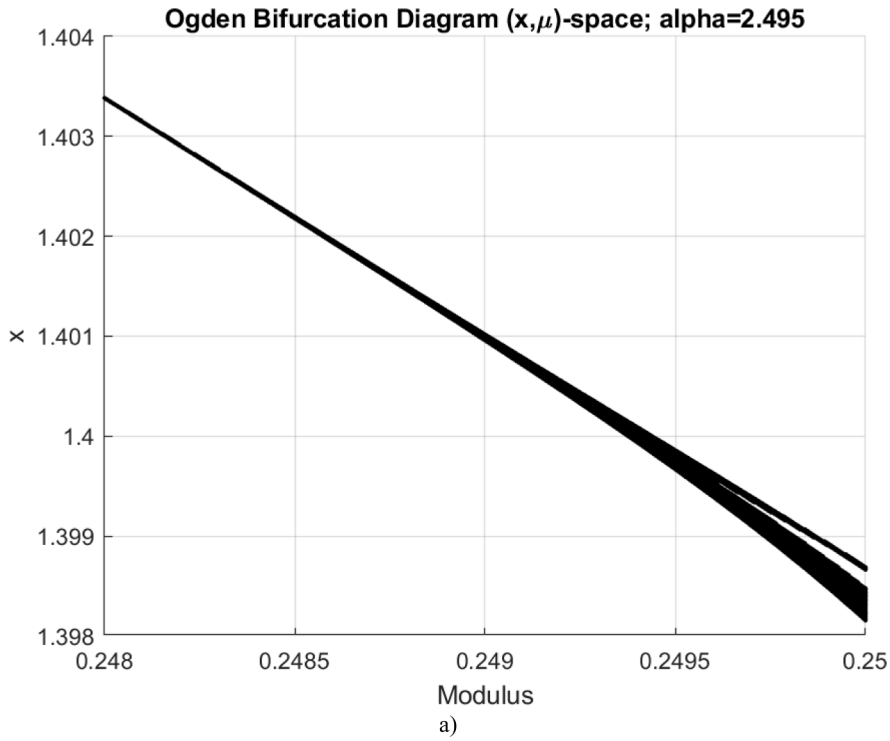


a)

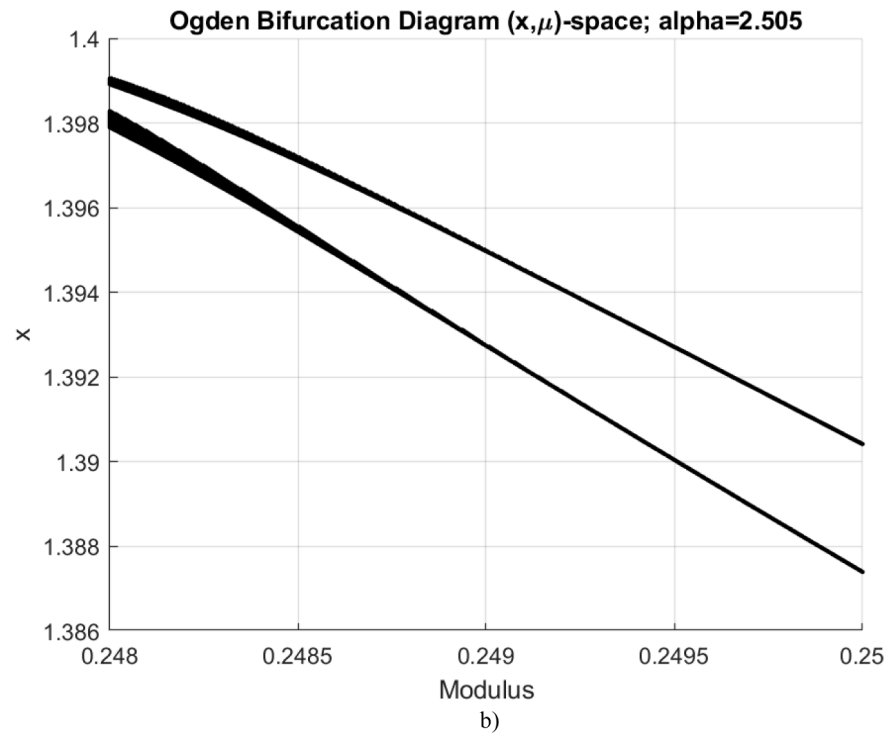


b)

Fig. 4. Bifurcation diagram in (x,μ)-plane s at viscosity variation: a) η=0.025; b) η=0.075.



a)



b)

Fig. 5. Bifurcation diagram in (x,μ)-plane s at Ogden exponent variation: a) α=2.49; b) α=2.55.

3. Numerical analysis

3.1. The model

3.1.1. Physical parameters

Consider a strong earthquake of intensity 10 on the MMI scale with a peak ground acceleration (PGA) of $0.8g \approx 7.85\, ms^{-2}$ at a dominant frequency 2.5 Hz [1–3,56]. This PGA value relates to a peak ground displacement (PGD) of approximately $3.2 \times 10^{-2}\, m$.

Following [10,57–59,12] consider hard rubber, modeled by a single-modulus Ogden model, specified by the following parameters

$$\mu = 10\, MPa; \alpha = 2.5 \tag{3.1}$$

Assume also a payload of $3,000\, kN$ on a seismic bearing with its square are of $2.0\ m^2$. These values are typical for high damping rubber bearings (HDRB) used in high-rise buildings or moderately large span bridges [12], yielding a mass element in Eq. (1.1) of $306,000\, kg$.

These parameters correspond to the following dimensionless parameters in Eq. (1.15)

$$\eta = 0.05; \mu = 0.3; \alpha = 2.5; u_0 = 0.06 \tag{3.2}$$

In the subsequent analysis, the dimensionless modulus μ is varied within the range

$$\mu \in [0.1;\ 1.0] \tag{3.3}$$

3.1.2. Computational parameters

A Poincaré section (stroboscopic map) for a bifurcation diagram is constructed by sampling the system's trajectory once per forcing period, thereby reducing the continuous-time dynamics to a discrete map that captures the long-term behavior of the oscillator. After integrating the system for a sufficiently long time to eliminate transients, the state is recorded at times $t=kT$, where T is the forcing period and $k=200\div300$ is a number of sampling periods. Plotting these sampled points as a function of a control parameter yields the bifurcation diagram: a single point indicates a period-1 orbit, a finite set of points corresponds to a period-n solution, a quasi-periodic regime forms a thin, continuous, non-fractal stripe whose thickness reflects the amplitude of the invariant torus, and a dense vertical band signals chaotic dynamics [60]. This stroboscopic sampling isolates the invariant structure of the forced system and provides a clear, parameter-dependent visualization of transitions between periodic, quasi-periodic, and chaotic regimes.

The accuracy of the bifurcation diagrams is ensured through long-time numerical integration with strict error control. All simulations are performed using a variable-step Adams–Bashforth–Moulton explicit–implicit scheme with local truncation error tolerances set to 10^{-12}, and multiprecision arithmetic is employed to avoid error accumulation over long trajectories. For each parameter value, transients corresponding to the first $500\div700$ cycles are discarded and the stroboscopic samples are taken only after the solution has reached its asymptotic regime. Convergence was verified by repeating selected simulations with tighter tolerances and higher precision, which produced indistinguishable diagrams.

3.2. Bifurcation diagrams

The bifurcation diagrams—defined as the vertical and horizontal projections on the phase coordinate axes of the Poincaré sections—are plotted over varying modulus (3.3); see Fig. 2.

Both bifurcation diagrams show the emergence of two regions of possible transition from stable, likely periodic motion, to another, apparently, periodic or quasi-periodic regime within the range $\mu \in [\sim 0.25;\ \sim 0.36]$; this regime is associated with a more complicated motion. A more detailed bifurcation diagrams in the vicinity of the first bifurcation region are shown in Fig. 3. Furthermore, what appear to be thin lines outside the suspected bifurcation regions in fact exhibit measurable thickness, suggesting dynamics more intricate than period-1 oscillations; see Fig. 3.

The large black regions in these bifurcation diagrams suggest the onset of chaotic motions and possibly quasi-periodic motions prior to chaos. Merging two chaotic regimes into a single one, most likely, correspond to a band-merging chaotic crisis [61,62]. A more detailed analysis of the nature of the motion—including phase portraits, Poincaré sections, and power spectral densities—will be given in Section 3.3.

The influence of the viscosity parameter η on the bifurcation diagram in the (x,μ)-space and within range $\mu \in [0.248;\ 0.252]$ is shown in Fig. 4 for fixed $\alpha = 2.5$. The comparison shows that varying η within range 0.05 ± 0.002 produces substantial changes in the resulting bifurcation structure. This indicates that, in this regime, the qualitative dynamics of the system are highly sensitive to moderate variations in viscous damping. Notably, the bifurcation diagram in the (v,μ)-space exhibits similarly large variations, confirming that the qualitative structure of the dynamics undergoes significant changes under the same range of viscosity perturbations.

Fig. 5 illustrates how variations in the Ogden exponent α affect the bifurcation diagram in the (x,μ)-space within range $\mu \in [0.248;\ 0.252]$ and at fixed $\eta = 0.05$.

The plots in Fig. 5 demonstrate that even very small variations in the Ogden exponent $\alpha = 2.5 \pm 0.005$ produce pronounced changes in the resulting bifurcation diagrams. This sensitivity indicates that the Ogden exponent α plays a dominant role in shaping the global dynamics, making the system highly responsive to even minute modifications of this parameter.

3.3. Phase portraits, Poincaré sections, and power spectral densities

To more precisely characterize the motion related to bifurcation diagrams shown in Fig. 2, consider three main regions within the entire range of μ-variation: (i) apparently, stable periodic regimes at $\mu \in [0.1;\ \sim 0.2] \cup [\sim 0.4;\ 1]$; (ii) multi-periodic or quasi-periodic regime at $\mu \in [\sim 0.25;\ \sim 0.36]$; and (iii) apparent chaotic or quasi-periodic regime at

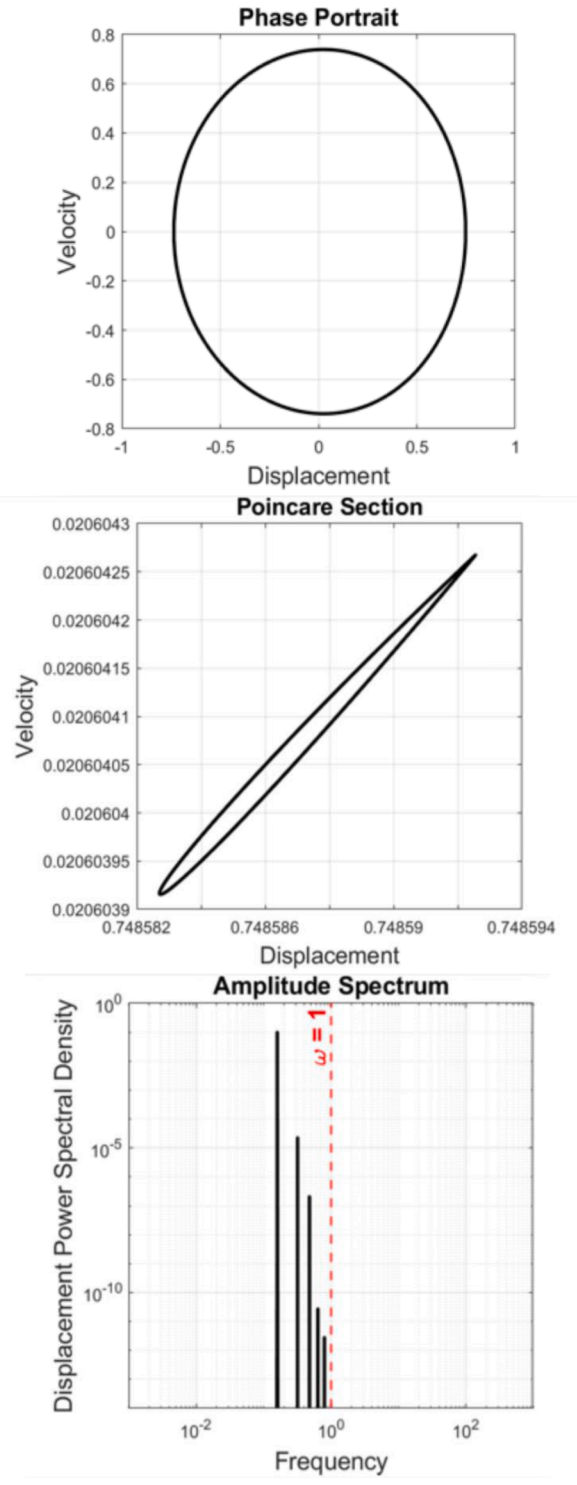


Fig. 6. First (periodic) regime; the red dotted line indicates the driving frequency via Ueda [36] normalization.

$\mu \in [\sim 0.2485;\ \sim 0.2495] \cup [\sim 0.368;\ \sim 0.374]$.

3.3.1. *Stable periodic regime*

The phase portrait, Poincaré section, and power spectral density related to $\mu = 0.8$, which belongs to the first regime, are shown in Fig. 6.

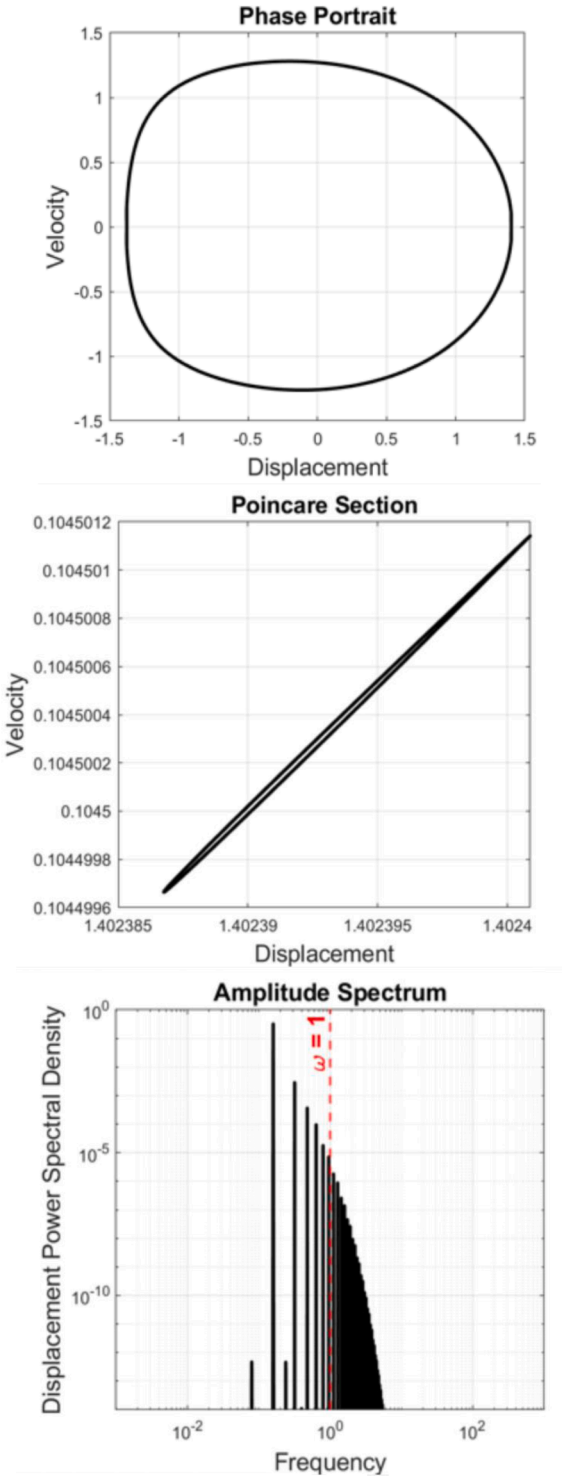


Fig. 7. Second (multi-periodic) regime; the red dotted line indicates the driving frequency via Ueda [36] normalization.

Thin closed loops in the phase portrait and Poincaré section, and, more importantly, a finite number of attenuating subharmonic amplitudes in the amplitude spectrum, suggest that the motion is period-5. This interpretation is supported by the spectrum itself, which contains five dominant spectral lines characteristic of a period-5 motion. Another observation concerns the occurrence of only subharmonic frequencies and the absence of the driving frequency—a phenomenon that can be dangerous for protected structures, since lower frequencies may induce larger amplitudes. The largest Lyapunov exponent (LLE) computed via the Rosenstein algorithm [63], yields $LLE = -0.12$, confirming the conclusion on periodicity.

3.3.2. *Multi-periodic regime*

Fig. 6 presents the phase portrait, Poincaré section, and power spectral density corresponding to $\mu = 0.3$, which belongs to the second regime.

Despite the visual similarity between phase portraits and Poincaré sections of the previous case and the current one, their amplitude spectra differ significantly. The amplitude spectrum in Fig. 7 contains both subharmonic and superharmonic. Furthermore, switching the frequency axis from logarithmic to linear scale, reveals the absence of incommensurate frequencies, as illustrated in Fig. 8.

This observation supports the hypothesis that the system exhibits multi-periodic rather than quasi-periodic motion. Computing the LLE for the considered case, yields $LLE = -0.03$, confirming the supposition of multi-periodicity.

3.3.3. *Chaotic regime*

Fig. 9 presents the plots of the phase portrait, Poincaré section, and power spectral density corresponding to μ, belonging to the third regime.

Strange attractor appeared in Poincaré section along with dense amplitude spectrum, containing both subharmonic and superharmonic components, may suggest the occurrence of chaos. Again, switching the frequency axis from logarithmic to linear scale in the amplitude spectrum plot reveals the emergence of a continuous spectral component—a hallmark of chaos; see Fig. 10.

Computing the LLE for the considered case, yields $LLE = 0.02$, indicating the emergence of chaotic dynamics.

4. Concluding remarks

This study has demonstrated that the modified nonlinear Kelvin–Voigt oscillator with an Ogden-type hyperelastic spring—representative of elastomeric seismic bearings—can exhibit chaotic vibrational behavior under specific excitation conditions. Through numerical integration of the governing autonomous system using the Adams–Bashforth–Moulton predictor–corrector scheme, the analysis revealed the presence of pronounced subharmonic, superharmonic, and broadband continuous spectral components, indicative of complex nonlinear dynamics. These chaotic features have significant implications for the performance of seismic isolation systems, as they may enhance structural motion and undermine the intended damping and protective functions of rubber-based isolators. A potential limitation of this study is that the analysis relies exclusively on the Ogden hyperelastic potential within an idealized oscillator model, which may not fully capture the broader complexity of nonlinear rubber elasticity present in practical

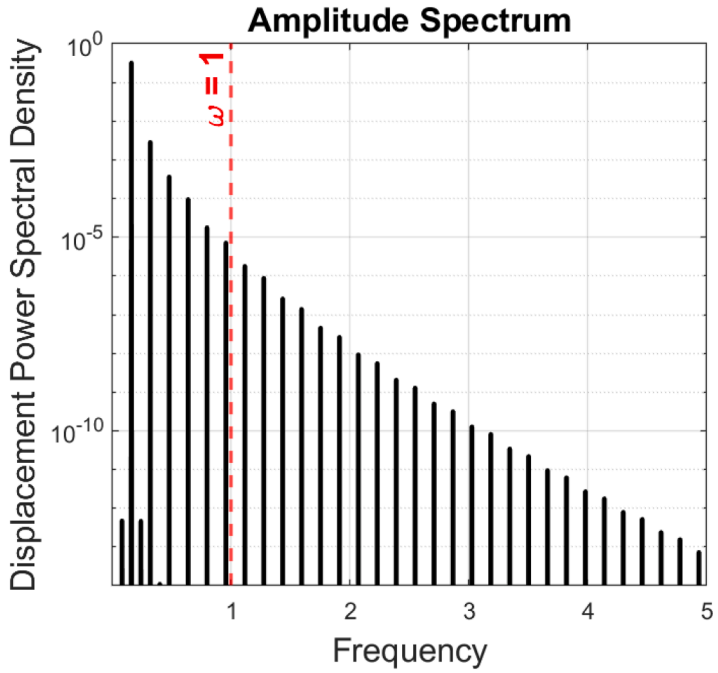


Fig. 8. Amplitude spectrum in semi-log coordinate.

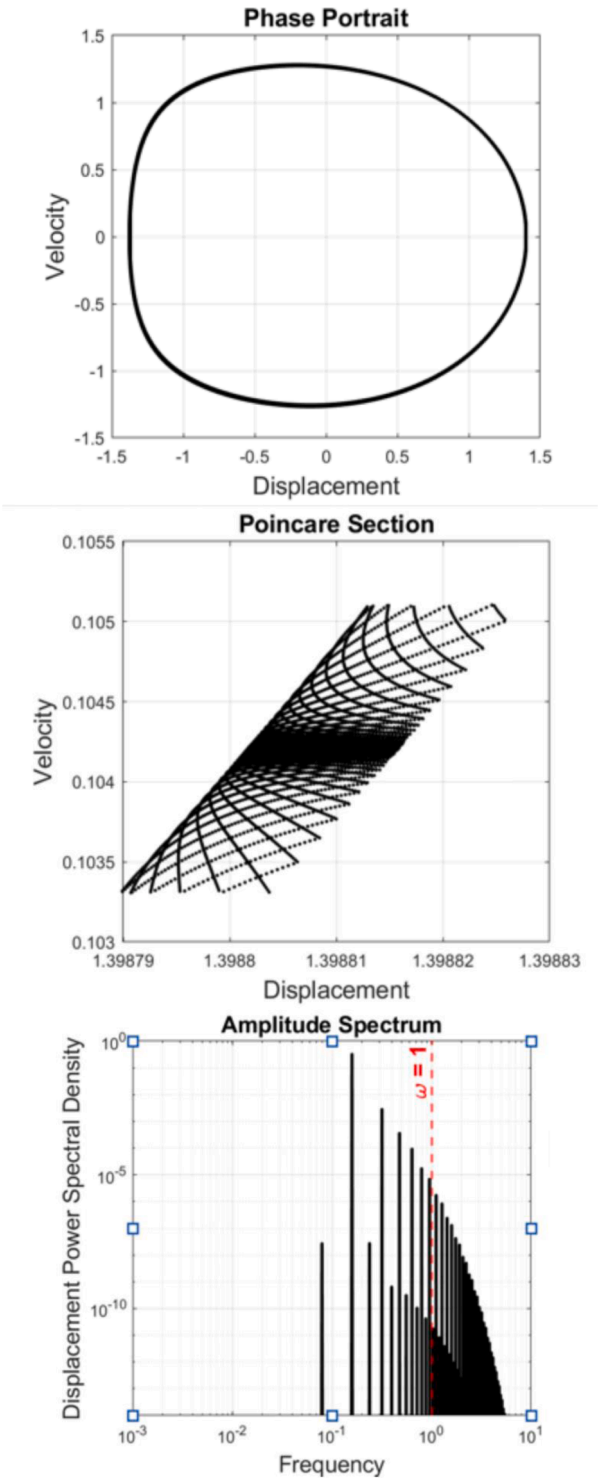


Fig. 9. Third (chaotic) regime; the red dotted line indicates the driving frequency via Ueda [36] normalization.

isolation systems.

The findings underscore the critical role of nonlinear material modeling in accurately capturing the dynamic response of hyperelastic components. In particular, the use of Ogden potentials enables a more realistic representation of the stiffness and energy dissipation characteristics inherent to hard rubber materials. By identifying regimes of chaotic and multi-periodic behavior, this work contributes to a deeper understanding of the vibrational stability of elastomeric isolation devices and highlights the necessity of

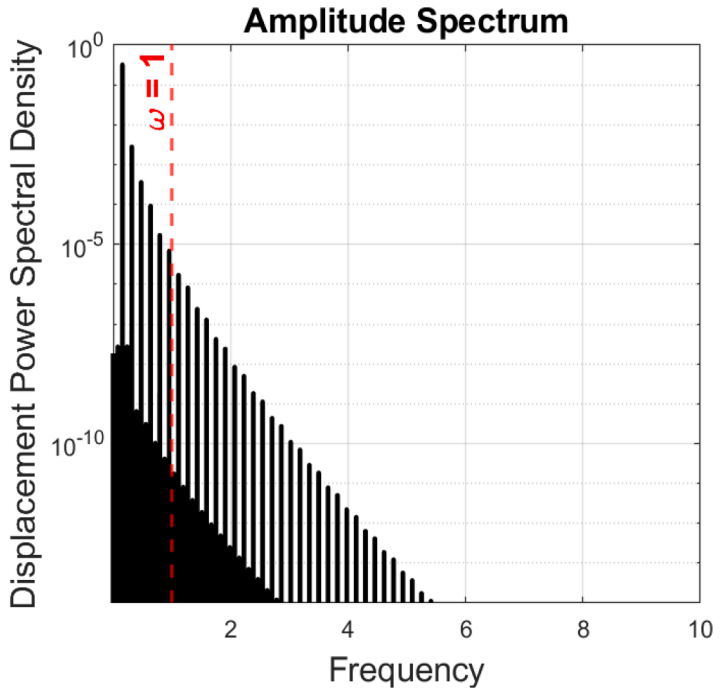


Fig. 10. Amplitude spectrum in semi-log coordinate.

incorporating nonlinear constitutive laws in the design and analysis of protective structural systems. One of the most promising directions for future work appears to be the incorporation of historical earthquake response spectra [64,65] in place of the considered forced harmonic oscillations.

Research involving human participants and/or animals

This article does not contain any studies with human participants and/or animals.

Informed consent

The author confirms knowledge of what this study involves.

CRediT authorship contribution statement

Vladimir Bratov: Writing – review & editing, Conceptualization. **Ashraf M. Iqbal:** Writing – original draft, Project administration. **Sergey V. Kuznetsov:** Software, Methodology, Investigation, Conceptualization.

Declaration of competing interest

The authors declare the following financial interests/personal relationships which may be considered as potential competing interests: Sergey Kuznetsov reports financial support was provided by Russian Science Foundation. If there are other authors, they declare that they have no known competing financial interests or personal relationships that could have appeared to influence the work reported in this paper.

Acknowledgments

The work (SVK) was supported by the Russian Science Foundation, Grant 24-49-02002.

Data availability

Data will be made available on request.

References

[1] Chopra AK. Dynamics of Structures: Theory and Applications to Earthquake Engineering. New Jersey: Prentice Hall; 1995.
[2] Clough RW, Penzien J. Dynamics of Structures. 2nd edition. New York: McGraw-Hill; 1993.
[3] Liu Y, et al. New equivalent linear impact model for simulation of seismic isolated structure pounding against moat wall. Shock and Vibration, 2014; 2014, 151237. Paper.
[4] Mavronicola EA, Polycarpou PC, Komodromos P. Effect of planar impact modeling on the pounding response of base-isolated buildings. Front Built Env 2016;2:11. Paper.
[5] Pagano D, Perna G, De Angelis M, Andreas U. Nonlinear dynamic response of the vibro-impact systems subjected to harmonic ground motion under conditions of uncertainty on the gap size. Int J Non-Linear Mech 2024;165(10):104816. Paper.
[6] Stefani G, De Angelis M, Andreas U. Numerical study on the response scenarios in a vibro-impact single-degree-of-freedom oscillator with two unilateral dissipative and deformable constraints. Comm Nonlinear Sci 2021;99(1,2):105818. Paper.
[7] Stefani G, De Angelis M, Andreas U. Exploit the study of the scenarios for the control of the response of single-degree-of-freedom systems with bumpers. J Sound Vibr 2024;578(10):118341. Paper.
[8] Guckenheimer J, Holmes P. Nonlinear Oscillations, Dynamical Systems, and Bifurcations of Vector Fields. New York, NY: Springer-Verlag; 1983.
[9] Bratov VA, Kuznetsov SV. Nonlinear shear waves in compressible media: occurrence of strong shocks. Math 2025;13(12):1–10.
[10] Dorfmann L, Merodio J, Penta R, Saxena P. In recognition of the 80th birthday of Ray Ogden. Math Mec Solids 2025;30(2):169–73.
[11] Kahle E, et al. Length scales in the tear resistance of soft tissues and elastomers: a comparative study based on computational models. Int J Fract 2025;249:27. Paper.
[12] Steck D, et al. Mechanical responses of Ecoflex silicone rubber: Compressible and incompressible behaviors. J Appl Polym Sci 2019;136:47025. Paper.
[13] Yao Y, Chen S, Huang Z. A generalized Ogden model for the compressibility of rubber-like solids. Phil Trans Roy Soc A 2022;380:2234. Paper.
[14] Ogden RW. Waves in isotropic elastic materials of Hadamard, Green, or harmonic type. J Mech Phys Solids 1970;18(2):149–63.
[15] Ogden RW. Large deformation isotropic elasticity – on the correlation of theory and experiment for incompressible rubberlike solids. Proc Roy Soc Lond Math Phys Sci 1972;326:565–84.
[16] Valanis KC, Landel RF. The strain-energy function of a hyperelastic material in terms of the extension ratios. J Appl Phys 1967;38:2997–3002.
[17] Connolly SJ, Mackenzie D, Gorash Y. Isotropic hyperelasticity in principal stretches: explicit elasticity tensors and numerical implementation. Comput Mech 2019;64:1273–88.
[18] Ehret AE, Stracuzzi A. Variations on Ogden's model: close and distant relatives. Philos Trans A Math Phys Eng Sci 2022;380(2234):20210322. paper.
[19] Korobeynikov SN. Generalized Ogden's incompressible isotropic hyperelastic material model supporting the form of Hooke's law. Arch Appl Mech 2025;95:105. Paper.
[20] Ogden RW. Nonlinear elastic deformations. Dover: Wiley; 1984.
[21] Ogden RW, Saccomandi G, Sgura I. Fitting hyperelastic models to experimental data. Comp Mech 2004;34(6):484–502.
[22] Storåkers B. On material representation and constitutive branching in finite compressible elasticity. J Mech Phys Solids 1986;34(2):125–45.
[23] Anssari-Benam A. Comparative modelling results between a separable and a non-separable form of principal stretches–based strain energy functions for a variety of isotropic incompressible soft solids: Ogden model compared with a parent model. Mech Soft Mater 2023;5. Paper 2.
[24] Destrade M, et al. Methodical fitting for mathematical models of rubber-like materials. Proc Roy Soc A: Math Phys Eng Sci 2017;473:20160811. Paper.
[25] Destrade M, et al. The Ogden model of rubber mechanics: 50 years of impact on nonlinear elasticity. Phil Trans R Soc A 2022;380:20210332. Paper.
[26] Destrade M, Dorfmann L, Saccomandi G. The Ogden model of rubber mechanics: 50 years of impact on nonlinear elasticity. Phil Trans R Soc A 2022;380:20210332. Paper.
[27] Ehret AE. On a molecular statistical basis for Ogden's model of rubber elasticity. J Mech Phys Solids 2015;78:249–68.
[28] Findik F, Yilmaz R, Köksal T. Investigation of mechanical and physical properties of several industrial rubbers. Mater Des 2004;25(4):269–76.
[29] Lohr MJ, et al. An introduction to the Ogden model in biomechanics: benefits, implementation tools and limitations. Phil Trans Roy Soc A 2022;380:20210365. Paper.
[30] Marckmann G, Verron E. Comparison of hyperelastic models for rubber-like materials. Rubber Chem Tech 2006;79(5):835–58.
[31] Rubin MB, Ehret AE. An invariant-based Ogden-type model for incompressible isotropic hyperelastic materials. J Elast 2016;125:63–71.
[32] Saedniya M, Talaeitaba SB. Numerical modeling of elastomeric seismic isolators for determining force–displacement curve from cyclic loading. Int J Adv Struct Eng 2019;11:361–76.
[33] Yamashita Y, Uematsu H, Tanoue S. Calculation of strain energy density function using Ogden model and Mooney–Rivlin model based on biaxial elongation experiments of silicone rubber. Polymers 2023;15(10):2266. Paper.
[34] Liu Y, Zhang L. Nonlinear static and dynamic behavior of elastomeric bearings for seismic isolation. Earthq Eng Struct Dyn 2004;33(8):1031–56.
[35] Kuznetsov SV. Infinitesimally small acoustic waves in hyperelastic media: appearance of shock waves and energy dissipation. Mech Adv Mater Struct 2025;2025:1–8.
[36] Ueda Y. Randomly transitional phenomena in the system governed by Duffing's equation. J Stat Phys 1979;20(2):181–96.
[37] Ueda Y. Explosion of strange attractors exhibited by Duffing's equation. Ann NY Acad Sci 1980;357:422–34.
[38] Ueda Y. Random phenomena resulting from non-linearity in the system described by Duffing's equation. Int J Non-Linear Mech 1985;20:481–91.
[39] Ueda Y. Survey of regular and chaotic phenomena in the forced Duffing oscillator. Chaos Solit Fractals 1991;1(3):199–231.
[40] Acharjee S, Dutta N, Devi R, Boruah A. Nonlinear oscillations, chaotic dynamics, and stability analysis of bilayer graphene-like structures. Chaos 2023;33(1):013136. Paper.
[41] Epstein IR, Pojman JA. An Introduction to Nonlinear Chemical Dynamics: Oscillations, Waves, Patterns, and Chaos. N.Y.: Oxford Academic; 2020.
[42] Negron-Marrero PV, Lopez-Serrano M. Minimal energy configurations of finite molecular arrays. Symmetry 2019;11:158. Paper.
[43] Showalter K, Epstein IR. From chemical systems to systems chemistry: Patterns in space and time. Chaos 2015;25(9):097613. Paper.
[44] Ghayesh MH. Nonlinear dynamic response of a simply-supported Kelvin–Voigt viscoelastic beam, additionally supported by a nonlinear spring. Nonlin Anal Real World App 2012;13(3):1319–33.
[45] Asnafi A. Chaotic analysis of Kelvin–Voigt viscoelastic plates under combined transverse periodic and white noise excitation: an analytic approach. Acta Mech 2020;231:139–54.
[46] Kurpa L, Pilgun G, Amabili M. Nonlinear vibrations of shallow shells with complex boundary: R-functions method and experiments. J Sound Vibr 2007;306:580–600.
[47] Hartman P. Ordinary Differential Equations. NY: Wiley; 1964.
[48] Hairer E, Nørsett SP, Wanner G. Solving Ordinary Differential Equations I: Nonstiff Problems. 2nd ed. Berlin: Springer-Verlag; 1993.
[49] Lambert JD. Numerical Methods for Ordinary Differential Systems: The Initial Value Problem. NY: Wiley; 1973.
[50] Kuznetsov SV. SH-waves in laminated plates. Quart Appl Math 2006;64:153–65.
[51] Li S, et al. Explicit/implicit multi-time step co-simulation in unbounded medium with Rayleigh damping and application for wave barrier. Eur J Env Civ Eng 2020;24:2400–21.
[52] Li S, et al. Benchmark for three-dimensional explicit asynchronous absorbing layers for ground wave propagation and wave barriers. Comp Geotech 2021;131:103808. Paper.
[53] Zhao B, Zhang B. Comparison of different order Adams-Bashforth methods in an atmospheric general circulation model. Acta Meteorol Sin 2011;25:754–64.
[54] Kuznetsov SV. Appearing ZGV point in the first flexural branch of Lamb waves in multilayered plates. Compos Struct 2022;290:115532. Paper.
[55] Il'yasov KK, et al. Exterior 3D Lamb problem: harmonic load distributed over a surface. Mech Solids 2016;51:39–45.
[56] Ma P, et al. Research status of relationship between seismic instrument intensity and ground motion parameters. IOP Conf Ser 2020;780:022002. Paper.

[57] Chagnon G, Rebouah M, Favier D. Hyperelastic energy densities for soft biological tissues: a review. J Elast 2015;120(2):129–60.
[58] Dudchenko AV. Vertical wave barriers for vibration reduction. Arch Appl Mech 2021;91:257–76.
[59] Martins PALS, Jorge RN, Ferreira AJM. A comparative study of several material models for rubber-like and elastomeric materials. Comp Mech 2006;40(2): 293–310.
[60] Strogatz SH. Nonlinear Dynamics and Chaos: With Applications to Physics, Biology, Chemistry, and Engineering. 2nd ed. USA: Westview Press; 2015.
[61] Avrutin V, Gardini L, Sushko I, Tramontana F. Continuous and Discontinuous Piecewise-Smooth One-Dimensional Maps: Invariant Sets and Bifurcation Structures, 95. NY: World Scientific; 2019. Nonlinear Science.
[62] Avrutin V, Panchuk A, Sushko I. Can a border collision bifurcation of a chaotic attractor lead to its expansion? Proc Roy Soc A 2023;479:2277. Paper.
[63] Rosenstein MT, Collins JJ, De Luca CJ. A practical method for calculating largest Lyapunov exponents from small data sets. Phys D: Nonlin Phenom 1993;65 (1–2):117–34.
[64] Blowes K, et al. Limiting safety-critical structural damage in recovery-based seismic design provisions. Earthq Spectra 2026;42:e70002. Paper.
[65] Damiani A, et al. Maximum usable period of ground motion records for engineering applications. Earthq Spectra 2026;42:e70003. Paper.